Research Paper

Smart tuning of 3D ordered electrocatalysts for enhanced oxygen reduction reaction

Yi-Fei Sun[a], Ya-Qian Zhang[a], Yan-Ling Yang[b], Jian Chen[c], Bin Hua[a,*], Yi-Xiang Shi[d], Chang-An Wang[e,*], Jing-Li Luo[a,*]

[a] Department of Chemical and Materials Engineering, University of Alberta, Edmonton, Alberta T6G 1H9, Canada
[b] State Key Laboratory of Physical Chemistry of Solid Surfaces, Xiamen University, Xiamen, Fujian 361003, China
[c] National Institution of Nanotechnology, National Research Council, Edmonton, Alberta T6G 2M9, Canada
[d] Key Laboratory for Thermal Science and Power Engineering of Ministry of Education, Tsinghua University, Beijing 100084, China
[e] School of Materials Science & Engineering, Tsinghua University, Beijing 100084, China

ARTICLE INFO

ABSTRACT

Extensive research has been devoted to the development of advanced oxygen reduction reaction (ORR) catalysts with functionally diverse active sites. Herein, we show a smart approach to advancing the ORR catalytic activity of a 3D porous perovskite. The facile oxidative-reductive-oxidative (O-R-O) thermal treatment cycle executed on Ag doped $LaFeO_3$ could stepwise switch on three different reaction sites (exsolved Ag-NPs, oxygen deficiency and Fe^{4+} with optimal electron configuration) for ORR. Detailed characterizations illustrate that the ORR activity is basically derived from the hierarchically porous scaffold which provides a large surface area and enough pore volumes for mass and ion diffusion. More importantly, the unique synergistic effects among three separate kinds of reaction sites endow the speed-up of oxygen adsorption, activation and O^{2-} transportation. The exemplified results set out new design principles for the optimization of alternative catalysts.

© 2017 Elsevier B.V. All rights reserved.

1. Introduction

For decades, the oxygen reduction reaction (ORR) has been paid paramount attention due to its centrality in various sustainable energy conversion and storage systems including, low temperature fuel cells for electricity generation and rechargeable metal-air batteries with high capacitance [1–3]. More specifically, it is imperative to look for a highly active and long-term durable oxygen electrode catalyst as the alternative to the state-of-art Pt/C electrocatalyst, which is limiting due to its scarcity and high price [4,5].

Basically, the perspective of structure engineering requires the resolution to structural barrier hampering ORR process, e.g., low surface area and poor porous structure [6,7]. The 3D marco-porous architectures were reported to show significantly increased electrochemical performance and stability for Li-O₂ batteries [8]. Such a well-ordered structure offered an enlarged interfacial area, modified diffusion tunnels for liquid electrolyte, accelerated transportation of fuel mass, and the rapid migration of electrons.

Undoubtedly, the intrinsic properties of many electrocatalysts exhibit more significant effects on the overall ORR performance. So far, diverse groups of electrocatalysts have been developed and investigated. Perovskite oxide (ABO_3 formula) family exhibits a fast oxygen diffusion rate [9–11] and its ORR activity is strongly related to the spin situations of electrons in the σ^*-orbital (e_g) of surface transition metal cations in the B-site [12]. An example of this conception is seen through the artificial introduction of an A-site deficiency into a $LaFeO_3$ perovskite, which in turn facilitated the creation of Fe^{4+} with an e_g orbital filling of 1. This has been proven to be the optimal electron configuration for boosting ORR activity [13]. Continued works on $LaNi_{1-x}Mg_xO_3$ in regard to ORR also illustrated the high ORR activity of $LaNiO_3$ by maintaining the oxidative state of Ni^{3+} with $e_g = 1$ [14].

A silver nanoparticle (Ag-NP) catalyst, as an alternative to the standard Pt/C catalyst, can function as a good metal based ORR electrocatalyst candidate (n-values near 4) with a more affordable price [15,17]. Due to its excellent oxygen solubility, electronic conductivity and catalytic activity, the Ag-NP catalyst showed desirable performance in terms of oxygen desorption, dissociation, diffusion and activation at both elevated and room temperatures [15,16]. Also, serving as an effective catalyst promoter, silver can be deposited onto perovskite oxides to enhance the electronic con-

ductivity and further optimize the intrinsic oxygen exchange rate for solid oxide fuel cells [17]. However, the application of Ag-NPs targeting ORR still has its challenges.

In order to achieve better performance, it is reasonable to propose the catalyst configuration which couples the merits of different types of developed catalysts. In contrast to traditional bi-functional or ternary ORR catalysts which deposit different components in a stepwise manner, we suggest fabricating the catalyst in a "one-pot" route and then gradually switching on each of the reaction sites via oxidative-reductive-oxidative (O-R-O) thermal treatment cycles from our pristine catalyst. the detailed schematic is shown in Scheme 1. (i) The ordered hollow framework, obtained through initial sintering, minimizes the impediments of mass and ions transportation within interpenetrated pathways, which in turn offers fundamental feasibility for highly efficient ORR processes. (ii) The exsolved Ag-NPs was further gained via the second-step *in-situ* reduction which has previously applied to the fabrication of diverse functional perovskite catalysts decorated with extraordinarily stable metallic NPs [18–22]. The exsolved Ag-NPs served as both active reaction sites and prime electron-transfer pathways. In addition, "pinned" Ag particles provide a strong anchoring force, effectively mitigating the instability of Ag. (iii) The tertiary thermal treatment step enables the reconstruction of an A-site deficient perovskite as Ag ions escape the perovskite lattice. Simultaneously, in order to keep the neutrality of the material, this oxidation step spontaneously tunes the oxidative state of Fe^{3+} to Fe^{4+} with an optimal σ^* orbital electron configuration, which further promotes ORR performance.

2. Results and discussion

Fig. 1(a) shows the X-ray diffraction (XRD) patterns of the as-synthesized $La_{0.95}Ag_{0.05}FeO_{3-\delta}$ based electrocatalyst powder. All samples, except LFA-500, exhibit diffraction peaks ascribed to the $LaFeO_3$ (PDF no. 37-1493), suggesting the crystallization of material could only be achieved while sintering above 500 °C. The exsolution of Ag from LFA-600 was first triggered in diluted 5% H_2/Ar at 400 °C for 2 h, where the exsolution temperature was determined based on hydrogen temperature programmed reduction (H_2-TPR) results of the 600-LFA sample (Figure S-1). Such low temperatures (i.e., 400 °C) were selected to protect the main perovskite lattice from

structural deconstruction. Following that, the sample was treated at 600 °C in an oxidative atmosphere for 3 h in order to restore the higher oxidative state of Fe. The sample still clearly shows diffraction peaks belonging to metallic silver at around 38.2 and 44.1° [17], indicating the preservation of Ag^0 after the O-R-O cycles.

The 3D ordered porous structure is considered to be a suitable nano-architecture for the electrode catalyst in metal-air batteries because of the facilitated mass transportation among its continuously interconnected micro-wall. The macroscopical morphologies of the as-prepared materials are identified using scanning electron microscopy (SEM) images. As the fabrication schematic illustration shown in Scheme 1, the long-term centrifugation enables the assembly of monodisperse spheres into close-packed arrays. The PMMA colloidal crystal template is impregnated with a precursor containing stoichiometric amounts of Fe^{3+}, La^{3+} and Ag^+ to form the as-prepared composite. After calcination, the close-packed sphere template (Fig. 1(b-1)) with a diameter of 200 nm (Fig. S-2) was removed and the three-dimensional (3D) well-ordered porous structure was successfully obtained while sintering at 600 °C (Fig. 1(b-2) and (b-3)). SEM imaging under high magnification illustrates the multi-layer structure (white arrows shown in Fig. 1(b-4) and Figure S-3(a)) with a highly ordered perpendicular alignment. The TEM images of the 600-LFA sample further demonstrate the first layer marcoporous structure with an average diameter of 200 nm stemming from the closed-packed monodisperse PMMA microsphere. The second layer of macrospores with a diameter of around 100 nm (Figure S-3(b)) are interconnected via a cubic-shape stub with 100 nm in diameter (Figure S-3(c)). The thicknesses of the wall at different orientations is around 50, 80 and 100 nm, varying with the particle–particle interaction extent. As shown in Figure S-4, the even element distribution of the 600-LFA sample across the porous framework was mapped by a STEM-EDS via integrating the electrical signal of La, Fe and Ag as a function of the beam position.

The resulting N_2 adsorption–desorption isotherms (Fig.1(c) and Figure S-5) provide evidence of the IV type isotherm for mesoporous 500-LFA, 600-LFA and T-600-LFA with the respective Brunauer–Emmett–Teller (BET) surface of 23.2, 24.1, and 23.4 $m^2 g^{-1}$ (shown in Figure S-6). For comparison, the 700-LFA, sintered at 700 °C, exhibited a decrease in its BET surface area with a value of only 11.5 $m^2 g^{-1}$, along with a destroyed porous struc-
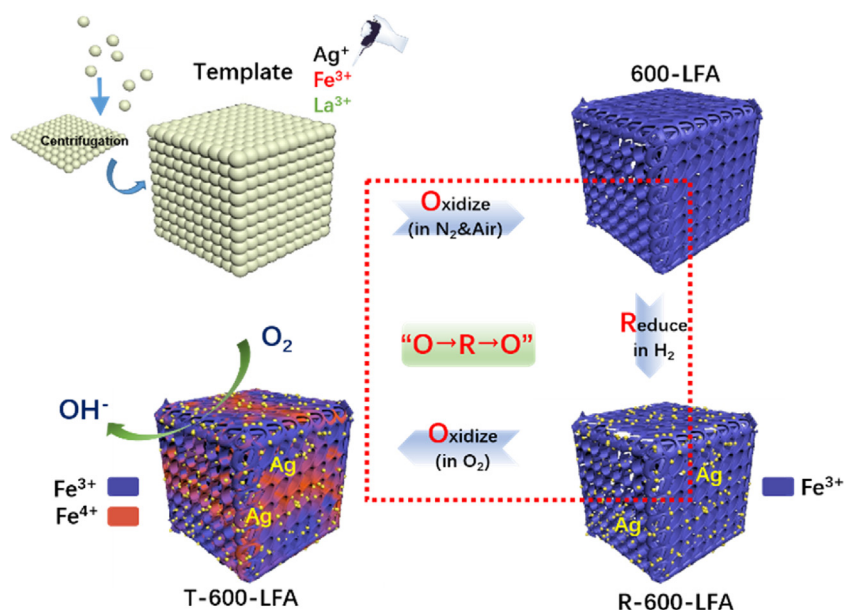
Scheme 1. Schematic illustration for preparation of 3D-Tuned LFA catalyst.
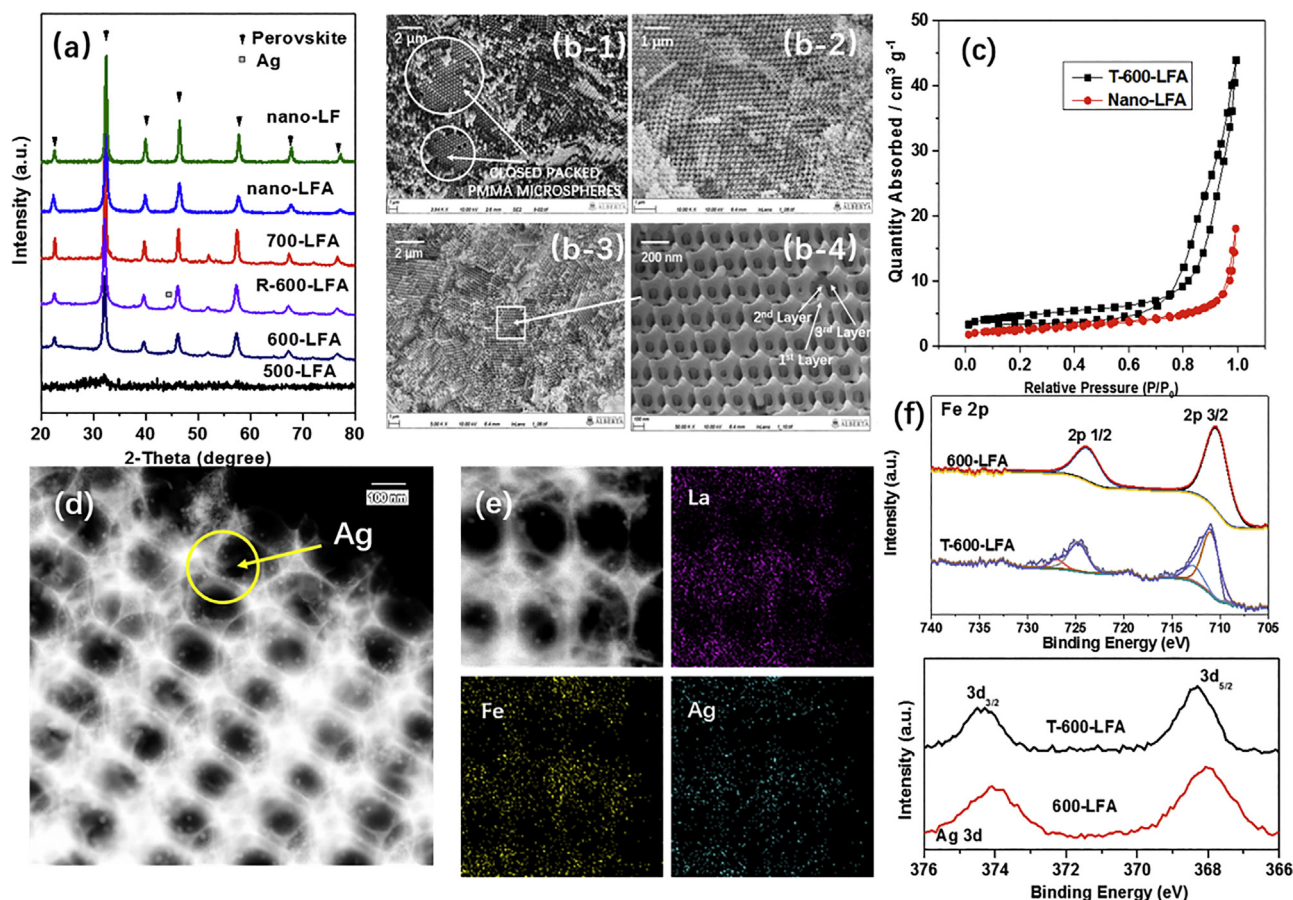
Fig. 1. (a) X-Ray diffraction patterns of various LFA catalysts; (b) SEM image of the closed-packed PMMA microsphere(b-1), SEM images of the 600-LFA sample (b-2 and b-3) and the high magnification SEM image of 600-LFA sample (b-4); (c) Nitrogen adsorption–desorption isotherms of different samples; (d) The STEM image of T-600-LFA sample; (e) STEM-EDS elemental mapping image for La, Fe, and Ag; (f) The XPS spectra of Fe 2p and Ag 3d of different catalysts.

ture and limited visual inter connected walls (Figure S-7). Nano-LFA with an average particle size of 200 nm was also synthesized. The BET surface area of the nano-LFA was calculated to be about $4.56 \, \text{m}^2 \, \text{g}^{-1}$. According to the BET surface area comparison, it seems as if further multiple-step treatment exhibits no obvious detrimental effect on the ordered porous structure. In agreement with the XRD patterns, the corresponding HAADF-STEM and EDX elemental mapping images (Fig. 1(d) and Fig. 1(e)) confirmed the anchoring of the homogeneously dispersed and segregated Ag (10 nm) on the maintained perovskite network.

It is reasonable to speculate that the pristine stoichiometric $La_{0.95}Ag_{0.05}FeO_{3-\delta}$ with certain amounts of exsolved Ag can be regarded as a non-stoichiometric perovskite with A-site cation deficiency ($xAg\text{-}La_{0.95}Ag_{0.05-x}FeO_{3-\delta}, 0 < x \leqq 0.05$). Comparing the slow scan rate XRD patterns of 600-LFA and T-LFA-600 (Fig S-8) not only indicates the existence of metallic Ag after the two-step thermal treatment, but also illustrates a slight shift of the main peak for (110) to higher angles after third step of calcination. This suggests a shrinkage of the lattice volume, perhaps due to the creation of an A-site deficiency as well as the formation of Fe^{4+} with smaller ion radius [13].

Shao-Horn's theory explains that perovskite oxide ORR catalysts containing transition metals with an optimal e_g orbital filling of 1 should have the highest activity in the alkaline solution [12]. This conception was also successfully utilized to understand the oxidation state dependent Pd [23] and Fe based [13] perovskite catalysts. XPS characterization was applied to further confirm the oxidation state of Fe in pristine 600-LFA and T-600-LFA as well as the valence states of Ag of perovskites. On one hand, the Fe $_{2p3/2}$ and $2p_{1/2}$ bind-ing energies located at around 710.9 eV and 724.6 eV respectively, can be ascribed to the Fe^{3+} ion which is the predominant oxidation state in both samples (Fig. 1(f)). Simultaneously, a certain amount of Fe with high oxidation states located at 712.9 eV and 726.3 eV can be observed on T-600-LFA, positively shifting the spectrum to the higher binding energy range. On the other hand, the pristine sample obtains the Ag $_{3d5/2}$ peak at 367.9 eV, indicating its Ag^+ state. Reduction shifts the peak to 368.3 eV strongly suggesting a transformation to the metallic state.

The electrocatalytic activity of different ORR catalysts was performed by using a rotating disk electrode (RDE) in 0.1 M KOH solution. All potentials were referenced to a reversible Ag/AgCl electrode. Before conducting each experiment, pure oxygen was purged into the electrolyte for 30 min to saturate the solution. Cyclic voltammetry (CV) tests were initially performed at a scan rate of $10 \, \text{mV s}^{-1}$. As shown in Figure S-9, the T-600-LFA sample showed a good cathodic peak at −0.252 V, which was more positive than that of 600-LFA (−0.3 V). Fig. 2a shows the linear sweep voltammetry (LSV) curves of different catalyst candidates at 1600 rpm anda scan rate of $5 \, \text{mV s}^{-1}$. The T-600-LFA catalyst exhibited a much higher limiting current density (4.5 mA cm^{-2}) and more positive onset potential (−0.15 V vs Ag/AgCl) than both the pristine 600-LFA catalyst (−0.17 V) and 700-LFA catalyst (−0.18 V). The nano-LFA exhibited the worst performance among all candidates (−0.22 V). The above results indicate that the treatment alter the properties of the electrocatalyst. The LSV curves of each catalyst at different rotation speeds (400–2500 rpm) are shown in Figure S-10. The Koutecky-Levich (K-L) plots (Fig. 2b) and corresponding slope calculations give electron transfer numbers (n)
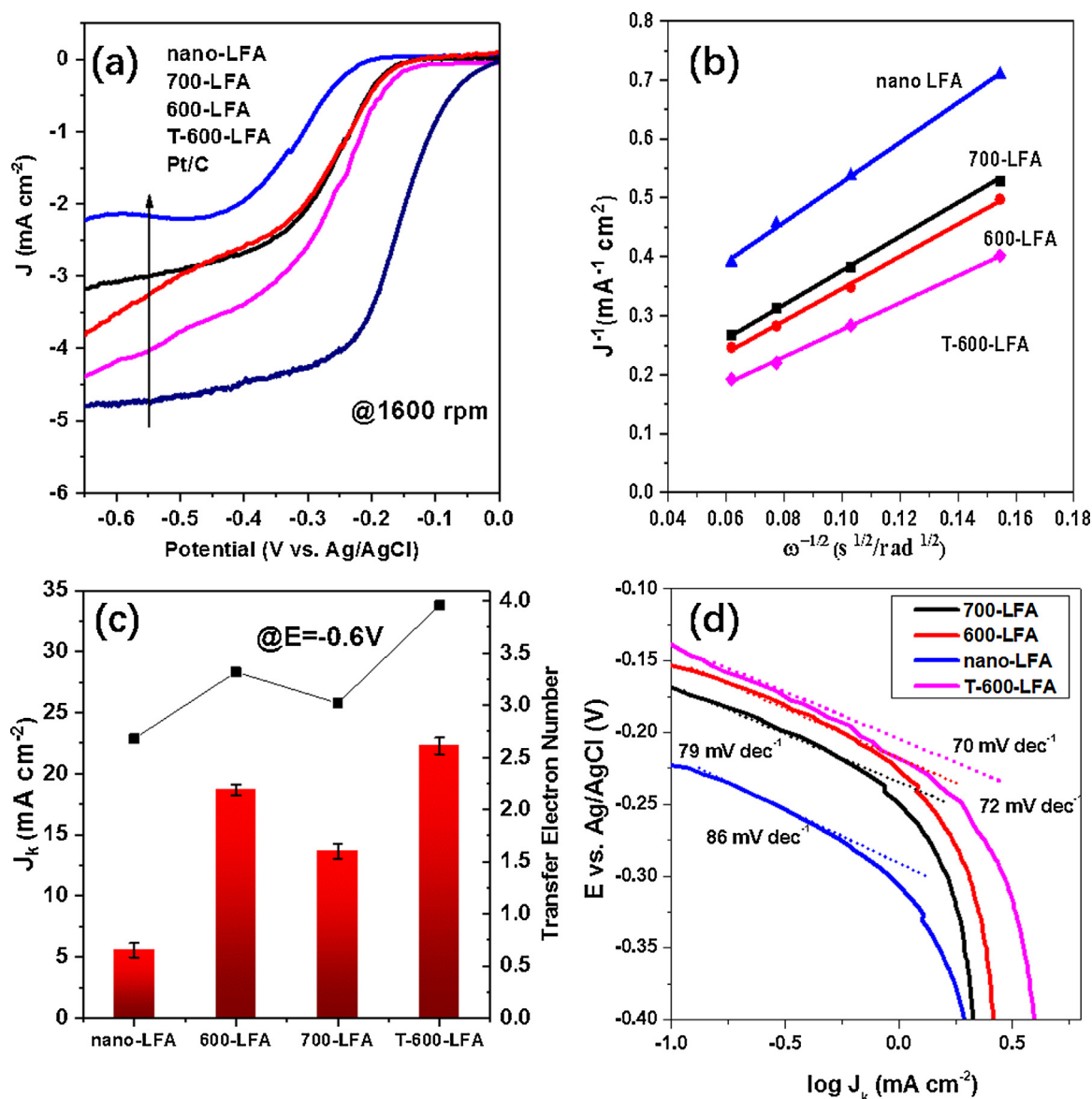
Fig. 2. (a) LSV curves for the ORR on the RDE (1600 rpm) on 20%Pt/C, LFA, 600-LFA, 700-LFA, and T-600-LFA catalysts in O_2-saturated 0.1 M KOH solution (scan rate: 5 mV s^{-1}); (b) K-L plots at −0.6 V for LFA, 600-LFA, 700-LFA, and T-600-LFA catalysts; (c) The electron transfer number (n) and kinetic current density (J_k)derived from the K-L plots at −0.6 V for LFA, 600-LFA, 700-LFA, and T-600-LFA catalysts; (d) Tafel plots of LFA, 600-LFA, 700-LFA, and T-600-LFA catalysts.

of −0.6 V is 2.68, 3.02, 3.32, and 3.96 for nano-LFA, 700-LFA, 600-LFA, and T-600-LFA, respectively (Fig. 2c). This result demonstrates that the 4-electron ORR process ($O_2 + H_2O + 4e- = 4OH^-$) is the dominant mechanism for T-600-LFA catalysts as compared to a 2-electron ORR process ($O_2 + H_2O + 2e- = HO_2^- + OH^-$, $HO_2^- + H_2O + 2e^- = 3OH^-$). Furthermore, the ORR activity of the catalysts can be reflected by other descriptors such as kinetic current density (J_k) shown in Fig. 2c and the Tafel plots shown in Fig. 2d. The J_k values at −0.6 V was 23 mA cm^{-2} for T-600-LFA material, which was higher than other competitors. The Tafel slopes for all porous LFA catalysts (70 mV dec^{-1}, 72 mV dec^{-1} and 79 mV dec^{-1} for T-600-LFA, 600-LFA and 700-LFA, respectively) are smaller than that of the nano-LFA catalyst (86 mV dec^{-1}), implying the 3D porous structure can apparently facilitate the electron transportation rate.

According to the above analysis, we propose the following reaction mechanism for the ORR occurring on our tuned catalyst. The possible reaction pathways for the catalyst with the O-R-O treatment is shown in Fig. 3 and diverse factors are generalized to collectively result in high ORR performance. Firstly, the 3D ordered

porous skeleton with large BET surface area provides a crack-free pathway for fast electrolyte solution transportation and ionic diffusion rate. Consequently, the resistance of gas diffusion can be ignored. The pristine $La_{0.95}Ag_{0.05}FeO_{3-\delta}$ has well distributed oxidative Ag ions within lattice which is not favorable in terms of the ORR. In order to gain surface decoration of metallic Ag NPs, the reduction treatment was applied to the catalyst. Preliminary research of ORR with Ag materials indicated that smaller Ag nanoclusters exhibit higher catalytic performance for ORR catalysis than Ag NPs with a larger diameter [24]. The exsolved nano-scale Ag provides a perfect 4-electron transfer process, hindering the formation of a byproduct of H_2O_2 and simultaneously benefiting the electron transportation. Also, the adsorption of O_2 can be improved due to Ag NPs as the extended adsorption zone. On the other hand, the catalytically active Fe^{4+} species tend to be reduced upon the reduction treatment process, negatively affecting the whole performance. Consequently, we re-oxidized this reduced catalyst to reconstruct the A-site deficient perovskite $La_{0.95}FeO_{3-\delta}$, shifting a certain proportion of B-site transition-metal ions to unstable
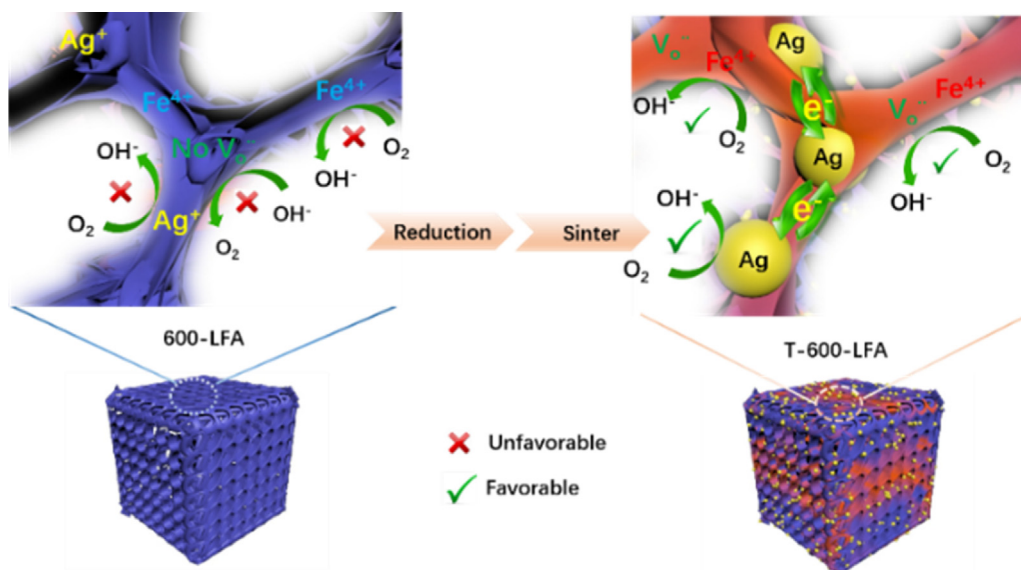
Fig. 3. Evolution of catalysts through a reduction-oxidation cycle to form multiple active reaction sites on the surface.

oxidation states (e.g., restore the surface Fe^{4+} species (as confirmed by XPS results in Figure S-10)). Completion of the O-R-O cycle reconstructed the A-site deficient perovskite with a certain amount of oxygen vacancies and Fe^{4+}. The existence of oxygen vacancies in A-site deficient perovskite could act as valid sites for binding oxygen, and could enhance the electronic conductivity and ionic mitigation [25,26]. It is worthy noticing that the exsolved Ag will maintain its oxidative state under the second-step sintering condition [16,17], preserving the Ag species catalytic activity. Therefore, the oxygen reduction reaction may occur in parallel at all three different reaction sites. The unified above three beneficial factors are responsible for the intrinsically enhanced performance.

3. Conclusion

In summary, we synthesized a 3D ordered porous $La_{0.95}Ag_{0.05}FeO_{3-\delta}$ catalyst with a controlled pore size and subjected it to O-R-O heat treatment in order to stepwise expose diverse functional reaction sites. The highest ORR activity was shown by the composite containing decorated Ag-NPs on the perovskite backbone, a tuned oxidation state of Fe, and certain amount of oxygen vacancies. The distinguished performance should be ascribed to the interconnected wall which favors mass and ion transportation, the existence of a perfect 4-electron catalyst composed of uniformly dispersed Ag, Fe with an optimal e_g orbital filling of 1, as well as the oxygen vacancies for oxygen adsorption. Such a straightforward tuning approach can be generalized for future designs and used in preparation of ordered porous transition-metal oxides based perovskite catalyst with multiple catalytic sites.

Acknowledgements

Appendix A. Supplementary data

Supplementary data associated with this article can be found, in the online version, at http://dx.doi.org/10.1016/j.apcatb.2017.08.017.

References

[1] J.T. Mefford, X. Rong, A.M. Abakumov, W.G. Hardin, S. Dai, A.M. Kolpak, K.P. Johnston, K.J. Stevenson, Nat. Commun. 7 (2016) 11053.
[2] X. Tian, J. Luo, H. Nan, H. Zou, R. Chen, T. Shu, X. Li, Y. Li, H. Song, S. Liao, R.R. Adzic, J. Am. Chem. Soc. 138 (2016) 1575–1583.
[3] D.S. He, D. He, J. Wang, Y. Lin, P. Yin, X. Hong, Y. Wu, Y. Li, J. Am. Chem. Soc. 138 (2016) 1494–1497.
[4] T. Takeguchi, T. Yamanaka, H. Takahashi, H. Watanabe, T. Kuroki, H. Nakanishi, Y. Orikasa, Y. Uchimoto, H. Takano, N. Ohguri, M. Matsuda, T. Murota, K. Uosaki, W. Ueda, J. Am. Chem. Soc. 135 (2013) 11125–11130.
[5] J.-X. Feng, H. Xu, Y.-T. Dong, S.-H. Ye, Y.-X. Tong, G.-R. Li, Angew. Chem. Int. Ed. 55 (2016) 3694–3698.
[6] H. Arandiyan, H. Dai, J. Deng, Y. Liu, B. Bai, Y. Wang, X. Li, S. Xie, J. Li, J. Catal. 307 (2013) 327–339.
[7] Y. Liu, H. Dai, Y. Du, J. Deng, L. Zhang, Z. Zhao, Appl. Catal. B: Environ. 119–120 (2012) 20–31.
[8] J.-J. Xu, Z.-L. Wang, D. Xu, F.-Z. Meng, X.-B. Zhang, Energy Environ. Sci. 7 (2014) 2213.
[9] F. Lu, J. Sui, J. Su, C. Jin, M. Shen, R. Yang, J. Power Sources 271 (2014) 55–59.
[10] J. Sunarso, A.A.J. Torriero, W. Zhou, P.C. Howlett, M. Forsyth, J. Phys. Chem. C 116 (2012) 5827–5834.
[11] W. Zhou, J. Sunarso, Z.-G. Chen, L. Ge, J. Motuzas, J. Zou, G. Wang, A. Julbe, Z. Zhu, Energy Environ. Sci. 4 (2011) 872–875.
[12] J. Suntivich, H.A. Gasteiger, N. Yabuuchi, H. Nakanishi, J.B. Goodenough, Y. Shao-Horn, Nat. Chem. 3 (2011) 546–550.
[13] Y. Zhu, W. Zhou, J. Yu, Y. Chen, M. Liu, Z. Shao, Chem. Mater. 28 (2016) 1691–1697.
[14] Z. Du, P. Yang, L. Wang, Y. Lu, J.B. Goodenough, J. Zhang, D. Zhang, J. Power Sources 265 (2014) 91–96.
[15] P. Singh, D.A. Buttry, J. Phys. Chem. C 116 (2012) 10656–10663.
[16] Y. Zhu, W. Zhou, R. Ran, Y. Chen, Z. Shao, M. Liu, Nano Lett. 16 (2016) 512–518.
[17] W. Zhou, R. Ran, Z. Shao, R. Cai, W. Jin, N. Xu, J. Ahn, Electrochim. Acta 53 (2008) 4370–4380.
[18] D. Neagu, G. Tsekouras, D.N. Miller, H. Menard, J.T. Irvine, Nat. Chem. 5 (2013) 916–923.
[19] Y.-F. Sun, J.-H. Li, M.-N. Wang, B. Hua, J. Li, J.-L. Luo, J. Mater. Chem. A 3 (2015) 14625–14630.
[20] Y. Sun, J. Li, Y. Zeng, B.S. Amirkhiz, M. Wang, Y. Behnamian, J. Luo, J. Mater. Chem. A 3 (2015) 11048–11056.
[21] T.S. Oh, E.K. Rahani, D. Neagu, J.T. Irvine, V.B. Shenoy, R.J. Gorte, J.M. Vohs, J. Phys. Chem Lett. 6 (2015) 5106–5110.
[22] D. Neagu, T.S. Oh, D.N. Miller, H. Menard, S.M. Bukhari, S.R. Gamble, R.J. Gorte, J.M. Vohs, J.T. Irvine, Nat. Commun. 6 (2015) 8120.
[23] Y. Zhu, W. Zhou, Y. Chen, J. Yu, X. Xu, C. Su, M.O. Tadé, Z. Shao, Chem. Mater. 27 (2015) 3048–3054.
[24] Y. Lu, W. Chen, J. Power Sources 197 (2012) 107–110.
[25] C.-F. Chen, G. King, R.M. Dickerson, P.A. Papin, S. Gupta, W.R. Kellogg, G. Wu, Nano Energy 13 (2015) 423–432.
[26] R. Gao, Z. Li, X. Zhang, J. Zhang, Z. Hu, X. Liu, ACS Catal. 6 (2016) 400–406.